Abdelhakim Amine Djendara[1], *Mohamed El Amine Khiari*[2*], *Abdallah Benzaama*[2]

ANALYSIS OF THERMAL AND RESIDUAL STRESSES IN MULTILAYER WELDED STAINLESS-STEEL PIPES USING DEFLUX AND FILM SUBROUTINES

ANALIZA TERMIČKIH I ZAOSTALIH NAPONA U VIŠESLOJNO ZAVARENIM CEVIMA OD NERĐAJUĆEG ČELIKA KORIŠĆENJEM DEFLUX I FILM POTPROGRAMA

Originalni naučni rad / Original scientific paper
Rad primljen / Paper received: 19.01.2025
https://doi.org/10.69644/ivk-2025-03-0487

Adresa autora / Author's address:
[1] University of Science and Technology of Oran-Mohamed Boudiaf (USTO-MB)-Algeria
A.A. Djendara https://orcid.org/0009-0001-5736-306X ;
[2] National Polytechnic School of Oran-Maurice Audin-Algeria
M. El Amine Khiari https://orcid.org/0009-0009-9379-2038 ,
*email: mohamedelamine.khiari@gmail.com
A. Benzaama https://orcid.org/0000-0002-3564-6157

Keywords

- AISI 304 stainless steel
- residual stresses
- finite element method (FEM)
- multi-pass welding
- heat transfer

Abstract

The study provides a comprehensive analysis of the impact of welding parameters, specifically welding speed and the number of passes, on the residual stress distribution in AISI 304 (Z7CN18-09) austenitic stainless steel tubes. A three-dimensional finite element model (FEM) is developed in ABAQUS® to simulate the circumferential welding process. DFLUX and FILM subroutines are employed to represent double-ellipsoid moving heat source and thermal boundary conditions, respectively. Model validation is achieved by comparing simulated weld bead profiles and thermal cycles with experimental data, yielding excellent agreement (deviation < 5 %).

The coupled thermal-mechanical analysis enables the evaluation of the spatiotemporal evolution of the temperature field at various welding speeds (80, 160, and 240 mm/min) and the distribution of axial and circumferential residual stresses across the tube thickness. The numerical results highlight the significant influence of welding parameters on the magnitude and distribution of residual stresses. Optimised welding speeds are shown to reduce maximum stress levels, while multi-pass welding improves stress homogenisation.

Ključne reči

- AISI 304 nerđajući čelik
- zaostali naponi
- metoda konačnih elemenata (FEM)
- višeslojno zavarivanje
- prenos toplote

Izvod

Ovaj rad daje sveobuhvatnu analizu uticaja parametara zavarivanja, konkretno brzine zavarivanja i broja prolaza, na raspodelu zaostalih napona u cevima od austenitnog nerđajućeg čelika AISI 304 (Z7CN18-09). Razvijen je trodimenzionalni model metode konačnih elemenata (FEM) u ABAQUS®-u za simulaciju procesa cirkularnog zavarivanja. Potprogrami DFLUX i FILM korišćeni su za predstavljanje dvostrukog elipsoidnog pokretnog izvora toplote i termičkih graničnih uslova. Validacija modela izvršena je upoređivanjem simuliranih profila šavova i termičkih ciklusa sa eksperimentalnim podacima, što pokazuje izuzetno poklapanje (devijacija < 5 %).

Spregnuta termičko-mehanička analiza omogućuje procenu prostorno-vremenskog razvoja temperaturnog polja pri različitim brzinama zavarivanja (80, 160 i 240 mm/min) i raspodelu aksijalnih i cirkularnih zaostalih napona po debljini cevi. Numerički rezultati ističu značajan uticaj parametara zavarivanja na veličinu i raspodelu zaostalih napona. Optimizovane brzine zavarivanja pokazuju smanjenje maksimalnih nivoa napona, dok višeprolazno zavarivanje poboljšava ujednačavanje napona.

INTRODUCTION

Welding, a fundamental assembly process in industry, encompasses various techniques broadly categorised based on their heat source into arc-based and beam-based processes. Among these, TIG (Tungsten Inert Gas) welding is particularly favoured for critical applications, such as in the nuclear industry, due to its high reliability and precision. Despite its widespread use, TIG welding has certain limitations, including high heat input requirements that necessitate groove preparation and multiple passes for thicker materials. These factors result in significant residual stresses, which can adversely affect the performance and durability of welded components. Such stresses are especially critical in the heat-affected zone (HAZ), where peak residual stress values are observed /1/.

Extensive studies have highlighted various factors influencing the intensity and distribution of residual stresses, including heat input and the number of passes /1, 2/, weld geometry /3/, material properties and microstructural changes /4/, as well as specific process parameters /5/. Finite element modelling (FEM) has proven to be an indispensable tool for predicting and analysing these stresses, with recent findings establishing the superiority of 3D models over 2D models /6, 7/. Smith et al. /8/ demonstrates that 3D models offer more accurate and realistic stress predictions for multi-pass welding of stainless-steel pipes, while Xu and Wang /9/ observe that residual stress values are higher in 3D models compared to 2D axisymmetric models. Additionally, research by Deng and Murakawa /10/ confirm a strong correlation between 3D FEM predictions and experimental observations for residual stresses and temperature cycles.

Recent advancements have shown that welding speed and heat input have a greater effect on circumferential stresses than on axial stresses, and that three-pass welding generates significantly lower stresses than two-pass procedures /11/. Genchev et al. /12/ further report that increasing heat input in thin-walled pipe welding raises the maximum HAZ temperature and expands the weld pool root. In the context of fast reactors, austenitic stainless steel AISI 304 is commonly employed for sodium transport pipes due to its superior mechanical properties and corrosion resistance.

Welded assemblies are critical elements in many industrial applications, requiring thorough analysis of their mechanical behaviour and reliability. In this context, the significant work of Djordjević et al. /15/ has considerably enriched our understanding of challenges related to welded joints. Their research covers a wide range of aspects, from multiple defect analysis to the study of innovative characterisation methodologies. Particularly relevant is their most recent study on numerical analysis of different weld geometries in lap joints of ammonia transport tanks /13/, along with their investigation of the influence of multiple defects in welded joints under fatigue loading, in accordance with SIST EN ISO 5817:2014 /14/. These studies have significantly enhanced our understanding of factors affecting the performance and durability of welded joints under real-world conditions. Their research on stereometric methods for measuring strains and displacements in welded joints under tensile loads /15/ provide valuable data for validating numerical models. The team also made notable advances in numerical and metallographic analysis of welded joints with root microcracks /16/.

Their earlier work on inverse iterative methodology for characterising welded joints in construction design demonstrates significant advantages compared to classical approaches /17/. Additionally, their foundational study on failure analysis of welded joints with multiple defects, using the extended finite element method and critical engineering analysis /18/ establishes a robust methodological framework for evaluating the structural integrity of complex welds. This method is also used by Khiari et al. /19, 20/.

This study focuses on numerically analysing residual stresses in these tubes, particularly evaluating the influence of welding parameters (welding speed and pipe thickness) on stress distribution. Using three-dimensional finite element modelling in ABAQUS®, DFLUX and FILM subroutines simulate the double-ellipsoid mobile heat source and thermal boundary conditions, respectively. Coupled thermal and mechanical analyses assess the spatiotemporal evolution of temperature fields across different welding speeds (80-160-240 mm/min) and the distribution of axial and circumferential stresses relative to tube thickness. This novel approach enables optimisation of welding parameters to reduce residual stresses, thereby improving the quality of welded assemblies and advancing the understanding of austenitic stainless-steel welding for critical nuclear applications.

USED STRUCTURE GEOMETRY AND PROPERTY

The pipe, constructed from AISI 304 stainless steel, has an inner diameter of 115 mm, a thickness of 6 mm, and length of 150 mm. Figure 1 depicts the pipe dimensions along with the welding direction. A two-pass welding procedure is carried out to validate the developed FEM model, with welding conditions specified in Table 1.

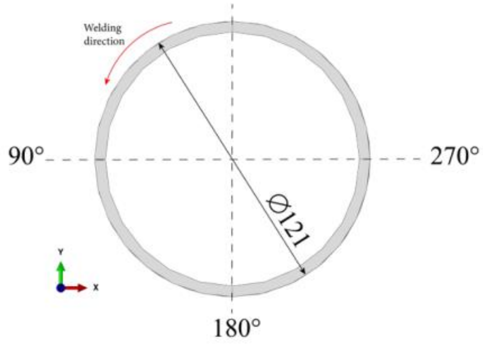

Figure 1. Pipe dimensions and welding direction.

The calculation of net heat input depends on arc energy multiplied by the arc efficiency, using the formula:

$$HI = \frac{\eta(60 \cdot I \cdot V)}{1000 \cdot v}, \tag{1}$$

where: η is welding efficiency (set at 80 %); I is welding current (A); V is welding voltage (V); v is welding feed velocity (mm/min); and HI is resulting heat input (kJ/mm).

Table 1. Welding condition for verifying experiments.

Pass no. 1	Voltage (V)	14.5	Welding speed (mm/min)	80
	Current (I)	105	Net heat input (kJ/mm)	0.913
Pass no. 2	Voltage (V)	14.5	Welding speed (mm/min)	80
	Current (I)	130	Net heat input (kJ/mm)	1.131

The welding setup consists of two pipes with specified dimensions, aligned side by side with a 2 mm gap between them. During the welding process, the pipes are automatically rotated at a constant speed. Temperature and residual stress measurements are taken at a 45° angle from the starting point. Each pipe undergoes two TIG welding passes, and the welded samples are subsequently analysed using X-ray diffraction (XRD) to assess residual stresses.

GOVERNING EQUATIONS

Thermal analysis

A transient heat transfer analysis in the welding region is performed relating to the equation:

$$\rho c \frac{\partial T}{\partial t}(x,y,z,t) = -\nabla \vec{q}(x,y,z,t) + Q(x,y,z,t), \tag{2}$$

where: ρ is material density; c is specific heat capacity; T is current temperature; ∇ is spatial gradient operator; q is heat flux vector; Q is internal heat generation rate; x, y, z are coordinates in the reference system; and t is time. The fundamental nonlinear isotropic Fourier heat flux equation is /11/:

$$\vec{q} = -k \nabla T \cdot \tag{3}$$

Here, k denotes the thermal conductivity, a parameter that varies with temperature. The heat generated by the welding arc is modelled using a volumetric heat source A based on the ellipsoid heat flux distribution, as described by Goldak's model (Fig. 2). This model ensures precise characterisation of the thermal input during the welding process (Velaga and Ravisankar) /11/. Front and rear heat sources are represented by Eqs. (4) and (5), respectively.

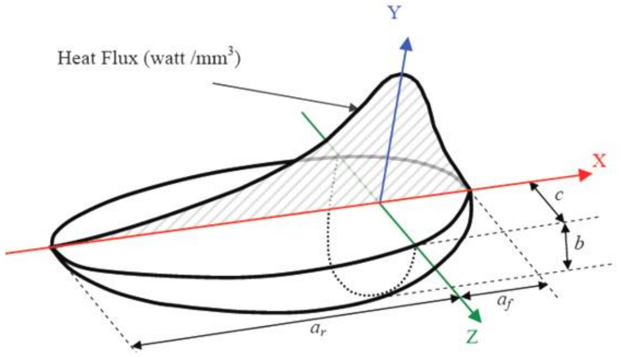

Figure 2. Heat source model.

$$Q(x',y',z',t')=\frac{6\sqrt{3}f_fQ_w}{a_fbc\pi\sqrt{\pi}}e^{-3x'^2/a_f^2}e^{-3y'^2/b^2}e^{-3z'^2/c^2}, \quad (4)$$

$$Q(x',y',z',t')=\frac{6\sqrt{3}f_rQ_w}{a_rbc\pi\sqrt{\pi}}e^{-3x'^2/a_r^2}e^{-3y'^2/b^2}e^{-3z'^2/c^2}, \quad (5)$$

where: x', y', z' are local coordinates of the double ellipsoid model.

The welded pipe is aligned such that the heat fraction is distributed between the front and rear regions, defined by f_f and f_r, respectively. It is important to note that $f_f + f_r = 2$. In this study, f_f and f_r are specified as 1.4 and 0.6, respectively, due to the steeper temperature gradient observed at the leading edge compared to the trailing edge of the weld path.

The power of the heat source Q_w is determined as a function of arc voltage, current, and welding efficiency. Parameters a_f, a_r, b, and c characterise the welding heat source and are crucial for defining its specifications, as described by Velaga and Ravisankar /11/.

The heat transfer coefficient, implemented via the FILM subroutine in the model, is described by Eq.(5). These parameters are critical for optimising conditions in the molten zone. At the welding surfaces, heat losses occur through both thermal radiation and heat transfer mechanisms.

In regions near the weld, where temperatures are high, radiation loss dominates. In contrast, farther from the weld region, where temperatures are cooler, convection becomes the primary heat loss mechanism. The thermal boundary conditions are simulated using a user-defined subroutine to accurately represent these processes.

$$h=\begin{cases}0.68T\cdot 10^{-8}\ (\mathrm{W/m^2}) & 0<T<500\ ^\circ\mathrm{C}\\ (0.231T-82.1)\cdot 10^{-16}\ (\mathrm{W/m^2}) & T>500\ ^\circ\mathrm{C}\end{cases} \quad (6)$$

The temperature (T) significantly affects thermal conductivity in various ways. When temperatures exceed the melting point, thermal conductivity is assumed to increase artificially several times higher than its room-temperature value to account for the enhanced heat transfer resulting from fluid flow within the weld pool.

The thermal boundary condition is initially applied to all free boundaries of the model during the first welding pass. During the second pass, it is extended to include the boundaries formed by the first pass. Additionally, the model incorporates the latent heat of fusion to account for the thermal effects during weld pool solidification.

For the AISI 304 pipe material used in this study, the specific values for latent heat, liquidus temperature, and solidus temperature are provided in Table 2.

Table 2. Latent heat and liquidus and solidus temperatures for AISI 304.

Material	AISI 304
Latent heat (kJ/kg)	260
Solidus temperature (°C)	1340
Liquids temperature (°C)	1390
Melting point (°C)	1365

Mechanical analysis

The mechanical analysis utilises temperature histories derived from thermal analysis. Under the assumption that no solid-state phase transformations occur in either the filler metal or the base metal, the total strain rate increment ($\dot{\varepsilon}$) can be decomposed into three components, as expressed in Eq.(7):

$$\dot{\varepsilon}=\dot{\varepsilon}^e\dot{\varepsilon}^p\dot{\varepsilon}^{th}, \quad (7)$$

where: $\dot{\varepsilon}^e$, $\dot{\varepsilon}^p$, $\dot{\varepsilon}^{th}$ represent elastic strain rate, plastic strain rate, and thermal strain rate, respectively. Equation (6) is applicable primarily for small plastic regions. The elastic strain is calculated using Hooke's isotropic law, incorporating a temperature-dependent Young's modulus as outlined in Eq.(6). These calculations rely on temperature-dependent mechanical properties listed in Table 3, including Young's modulus and Poisson's ratio.

First form (principal stresses):

$$\bar{s}=\sqrt{(s_1-s_2)^2+(s_2-s_3)^2+(s_3-s_1)^2}=s_y\,. \quad (8)$$

The combined model (yield function):

$$f=\bar{s}-[s_0+R_\infty(1-e^{b\dot{\varepsilon}_p})]=0\,, \quad (9)$$

where: σ is flow stress; σ_0 is initial yield stress; R_∞ is maximum change in yield stress (saturation value); b is the hardening rate parameter; and $\dot{\varepsilon}_p$ is equivalent plastic strain. This represents the yield condition where plastic deformation occurs when $f = 0$.

NUMERICAL METHOD

Finite element modelling

A FEM model is developed to accurately predict the temperature fields and residual stress distribution around the pipe weld line. Due to the negligible influence of dimensional variations and mechanical work in arc welding relative to the arc's thermal energy, a decoupled formulation is employed to simulate the thermomechanical behaviour of the weld metal.

This decoupled approach solves the thermal conduction problem independently of the stress field, although it accounts for thermal expansion, temperature-dependent thermophysical and thermomechanical properties, and the transient temperature field's influence on stress analysis.

The simulation process consists of two steps: first, a thermal analysis generates the temperature history. This thermal history is then applied as a thermal load to the relevant nodes during the mechanical analysis phase to evaluate the resulting residual stress field. Finally, the model is used to examine the effects of welding speed, heat input, and the number of welding passes on the internal and external surface stresses of the pipe.

The TIG welding simulation model is developed using ABAQUS coupled with FORTRAN codes. The weld design features a circular configuration around the pipe, with a coded transformation matrix to accurately represent the moving heat source. Surface temperature variations and heat transfer quantities are computed using the FILM subroutine, while the volumetric heat flux is modelled using the GOLDACK method.

The weld deposition process is simulated using the element birth and death method, effectively representing material addition during welding. Both radiation and convection heat transfer coefficients are incorporated into the model for accurate thermal analysis. The filler metal used in the TIG welding process is Y308L, chosen due to its compatibility with the base metal, as both exhibit nearly identical properties. Their temperature-dependent mechanical and thermal properties are detailed in Table 3. For temperatures exceeding 1500 °C, ABAQUS applies the properties specified for the highest temperature listed in the Table, /21/.

Table 3. Thermal, physical, and mechanical properties of AISI 304.

T (°C)	Spec. heat (J/kg°C)	Conduct. (W/m°C)	Density (kg/m^3)	Yield Stress (MPa)	Therm. exp. coef. (°C^{-1}) ×10^{-5}	Young's modulus (GPa)	Poisson ratio
0	462.0	14.6	7900	265.0	1.70	198.5	0.294
100	496.0	15.1	7880	218.0	1.74	193.0	0.295
200	512.0	16.1	7830	186.0	1.80	185.0	0.301
300	525.0	17.9	7790	170.0	1.86	176.0	0.318
400	540.0	18.0	7750	155.0	1.91	167.0	0.326
600	577.0	20.8	7660	149.0	1.96	159.0	0.333
800	604.0	23.9	7560	91.00	2.02	151.0	0.339
1200	676.0	32.2	7370	25.00	2.07	60.00	0.339
1300	692.0	33.7	7320	21.00	2.11	20.00	0.342
1500	700.0	120.0	7320	10.00	2.16	10.00	0.388

Meshing

The 3D finite element (FE) model, depicted in Fig. 3, consists of 9,360 elements and 12,150 nodes. Exploiting weld line symmetry, the model represents only one-half of the pipe, with results for temperature distribution and residual stress mirrored to reflect the entire geometry.

The mesh design incorporates gradient refinement, with finer elements (minimum size: 0.5 mm × 1.5 mm × 3.5 mm) concentrated near the weld line to capture detailed thermal and mechanical effects. Element sizes increase progressively with distance from the weld line to optimise computational efficiency. The modelled pipe dimensions are 150 mm in length, 127 mm in outer diameter, and 6 mm in thickness.

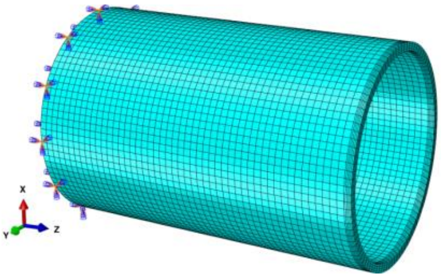

Figure 3. 3D model of the pipe and boundary conditions.

The welding simulation adopts a sequential pass strategy, defining distinct element zones corresponding to each welding pass. During the first pass simulation, elements assigned to the second pass remain inactive. After completing the first pass, these dormant elements are activated to simulate the second welding pass, ensuring the thermal and mechanical effects of the first pass are preserved.

The weld deposition process is modelled using the element birth and death method. Elements along the weld path are initially deactivated and are progressively activated to simulate the step-by-step fusion of the pipe material during welding.

Validation

The finite element model (FEM) for multi-pass TIG welding of stainless-steel pipes is validated through experimental comparison. The validation process involves an AISI 304 stainless steel pipe welded using a two-pass butt welding technique, with current values of 105 and 130 A for the first and second passes, respectively, as outlined in Table 1.

The model is first verified by comparing its predictions for temperature history and residual stress distribution with experimental measurements for the two-pass welded AISI 304 pipe. Following validation, the model is employed to analyse the effects of welding pass number, heat input, and welding speed on temperature history and residual stress distribution.

Validation of thermal history

The two-pass TIG welding conditions for the AISI 304 pipe are outlined in Table 2, with parameters specified individually for each pass. Both passes maintain a constant voltage of 14.5 V and a welding speed of 80 mm/min. Figure 4 displays the numerical temperature history curve at the weld centre, along with numerical and experimental temperature history curves measured at distances of 7 and 13 mm from the weld line for both passes. The results demonstrate good agreement between numerical and experimental temperature histories at these distances, validating the model's accuracy.

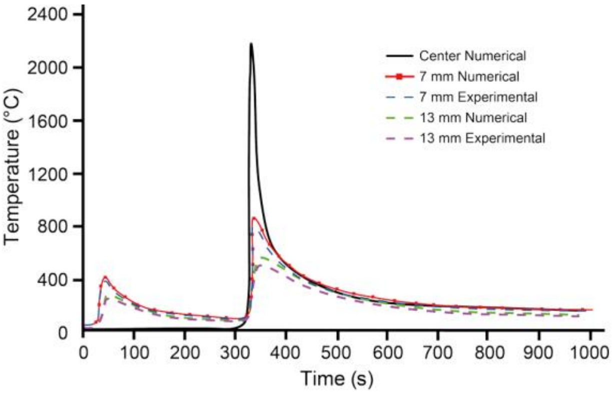

Figure 4. Time-temperature cycles for the first and second passes of TIG welding of AISI 304 at the pipe outer surface and distances of 7 and 13 mm from the weld line. Results are taken at the angle of 45° after the weld start. Welding speed: 80 mm/min.

These temperature history curves are recorded on the pipe's outer surface at specific weld points (0, 7, and 13 mm from the weld centre), which contribute to the development of residual stresses around the weld zone. The study examines axial and circumferential residual stresses on the welded pipe's inner and outer surfaces. These stresses arise due to the severe temperature variations during the welding thermal cycle, including heating, peak temperature, and cooling phases.

Temperature fluctuations significantly affect the filler metal and regions near the weld pool, particularly HAZ. The magnitude and distribution of residual stresses vary across different welding stages due to these thermal changes. Additionally, the outer surface's centre temperature remains at ambient levels before the second welding pass, as material deposition has yet to occur. Temperature curves in Fig. 4 highlight notable differences in peak temperatures at three measured locations, reflecting the dynamic thermal behaviour of the welding process.

Validation of residual stresses

Figures 5a-d illustrate excellent agreement between numerical and experimental results for both axial and circumferential residual stresses measured on inner and outer surfaces of the pipe. This validation confirms the reliability of the FEM in simulating multi-pass butt welding of stainless-steel pipes. The model demonstrates high accuracy in predicting both thermal and mechanical responses, further supporting its effectiveness in capturing the complexities of the welding process.

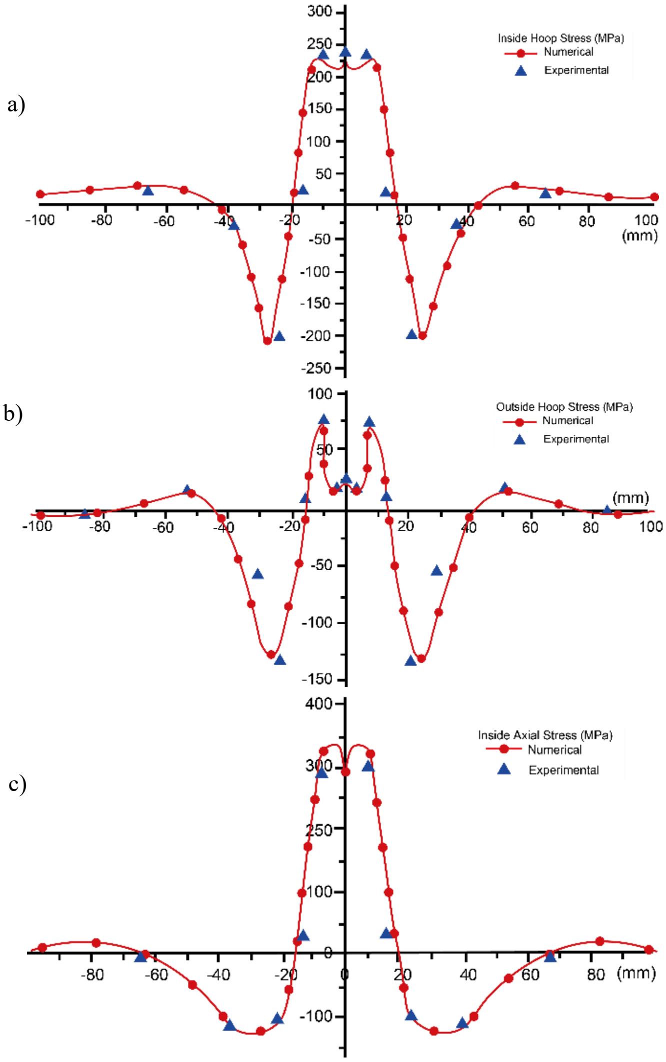

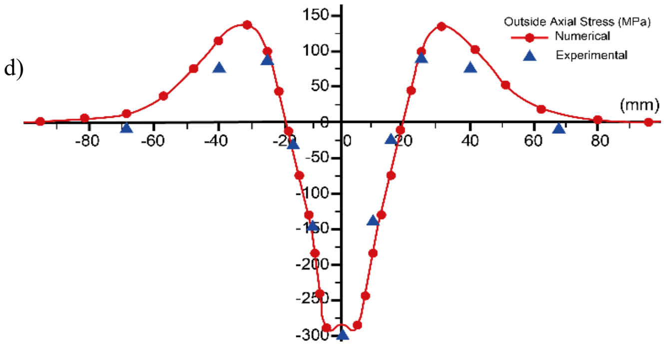

Figure 5. Comparison of stress results obtained from the numerical model and experiments: a) inside hoop stress; b) outside hoop stress; c) inside axial stress; d) outside axial stress. (Asadi et al. 2020) /22/.

RESULTS AND DISCUSSION

Following the validation of the numerical model, a detailed investigation is conducted to evaluate the influence of welding speed, heat input, and number of welding passes on residual stress distributions and temperature fields. The results of this analysis are presented and discussed in the subsequent subsections.

Validation

Experimental parameters for the multi-pass TIG welding of AISI 304 stainless steel pipes are summarised in Table 4, with distinct welding conditions specified for each pass in the two-pass procedure. Voltage is consistently maintained at 14.5 V across all welding operations, while current intensity and consequently the heat input are increased during the second pass.

Table 4. Welding conditions in the two-pass TIG welding of AISI 304 stainless steel pipe.

Pass no. 1	Voltage (V)	14.5	Welding speed for case 1 (mm/min)	80
	Current (I)	105	Welding speed for case 2 (mm/min)	0.913
Pass no. 2	Voltage (V)	14.5	Welding speed for case 2 (mm/min)	80
	Current (I)	130	Heat input for case (kJ/mm)	1.131

Three welding speeds are evaluated: Case 1 at 80 mm/min, Case 2 at 160 mm/min, and Case 3 at 240 mm/min. This systematic variation in welding parameters provides a comprehensive basis for analysing their effects on the thermal behaviour of the welded joint.

Figure 6 presents a detailed analysis of temperature distributions around the weld zone, illustrating thermal patterns when the heat source is positioned at a 45° angle from the second pass initiation point, across different welding speeds in two-pass welded specimens. The results show an inverse relationship between welding speed and peak temperature in two-pass welds, which is attributed to the reduced heat input at higher welding speeds.

This correlation can be explained by the decreased volume of filler metal deposited per pass, resulting in a more concentrated heat input at each point during the welding process. Consequently, the residual stresses that develop can either be tensile or compressive, depending on the type and location of non-uniform volumetric changes. These changes occur simultaneously at both macroscopic and microscopic levels, influencing the overall stress distribution.

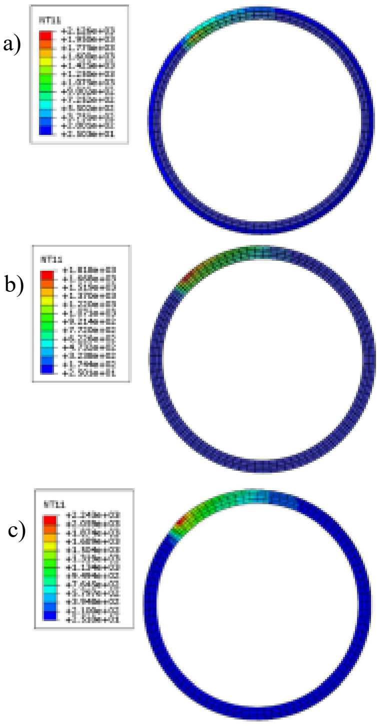

Figure 6. Temperature distribution around the weld line at 45° after the start point of two-pass welding. Welding speeds: a) 80, b) 160, and c) 240 mm/min.

Temperature distribution analyses across the weld cross-section are presented in Fig. 7, showing maximum thermal profiles for both the initial and subsequent passes on pipe external and internal surfaces. Experimental data reveal an inverse relationship between welding speed and peak temperatures.

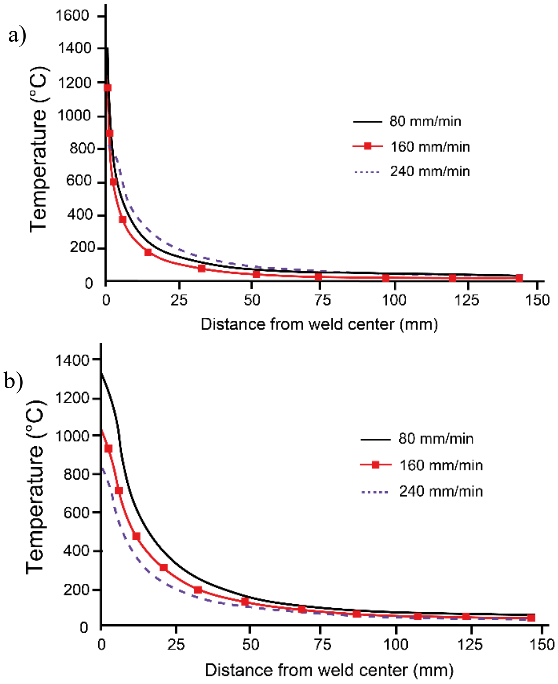

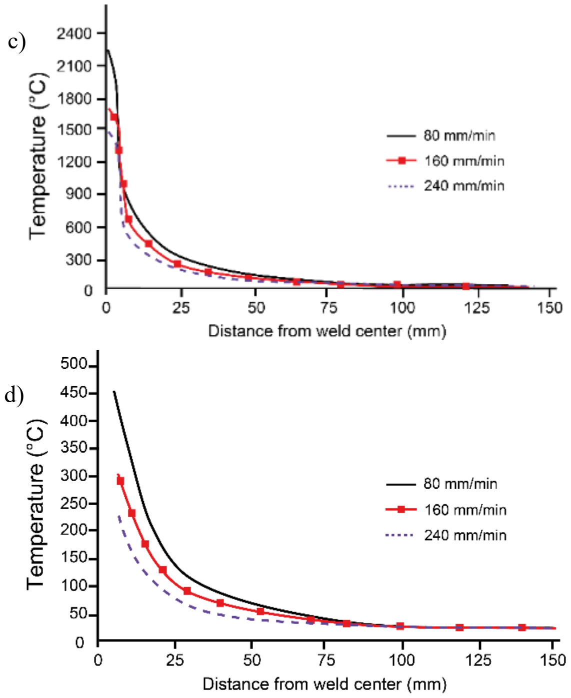

Figure 7. Peak temperature distribution with distance perpendicular to weld centreline for: a), b) inner surface; and c), d) outer surface; a), d) first pass; and b), c) second pass of the weld.

During the initial pass, the internal surface experiences significantly higher thermal loads, reaching 1400 °C at 80 mm/min, Fig. 7a. In contrast, a pronounced through-thickness thermal gradient is observed with temperature attenuation through the lower layers, resulting in internal surface temperatures of 1350 °C for specimens welded at 80 mm/min (Fig. 7b).

Subsequent pass generated temperatures exceeding the material's fusion point on the external surface, Fig. 7c, with peak values around 2200 °C for specimens welded at 80 mm/min, Fig. 7d. Specimens fabricated at 80 mm/min also exhibit a maximum temperature of 458 °C at a peripheral location away from the centreline, due to the absence of material at pipe exterior surface centre, resulting from direct arc impingement.

These thermal distributions align with the well-established heat transfer mechanisms in multi-pass welding operations, where heat input and material deposition progressively shape the thermal profile.

Residual stress analysis as a function of pipe thickness

Figure 8 presents the maximum residual stress profiles as a function of distance from weld centreline, incorporating detailed measurements of both axial and von Mises residual stresses on the external and internal surfaces at a 45° angle from the weld start position. This analysis covers three pipe thicknesses: 6 mm, 8 mm, and 10 mm.

The examination of axial stress patterns on the external surface, Fig. 8a, reveals compressive stresses at the weld centreline, which transits to tensile stress beyond 16 mm radially. As pipe thickness increases, there is an inverse relationship between tensile axial stress in HAZ and thickness, while compressive stress variations at the weld centre remain minimal. Specifically, as thickness increases from 6 to 10 mm, peak tensile axial stress decreases from 135 to 104 MPa, while the peak compressive stress decreases from 297 to 290 MPa. The narrowing of the residual stress-affected zone with greater thickness is attributed to improved heat dissipation due to the increased material volume.

Axial stress distribution on the internal surface, Fig. 8b, exhibits a complementary pattern, with tensile stress at the centre transitioning to compressive stress beyond 16 mm from the centreline. Thickness variation has minimal impact on the stress patterns, with slight reductions in peak tensile stress at weld centre. The peak tensile axial stress decreases slightly from 336 to 329 MPa as the thickness increases from 6 to 10 mm, while peak compressive stress remains relatively unchanged.

Von Mises residual stress distributions, Figs. 8 c and d, exhibit consistent thickness-dependent behaviour on both surfaces, with maximal stresses approaching yield strength of AISI 304 in thicker specimens. This is particularly noteworthy for structural integrity considerations, as high von Mises stresses may influence potential for material failure under loading.

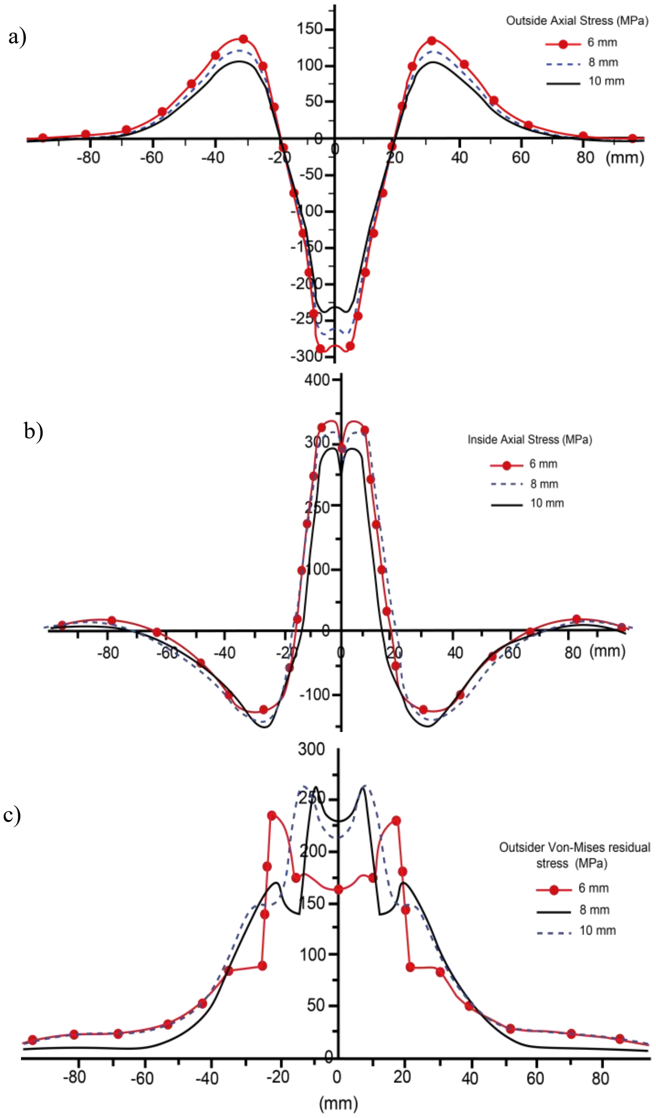

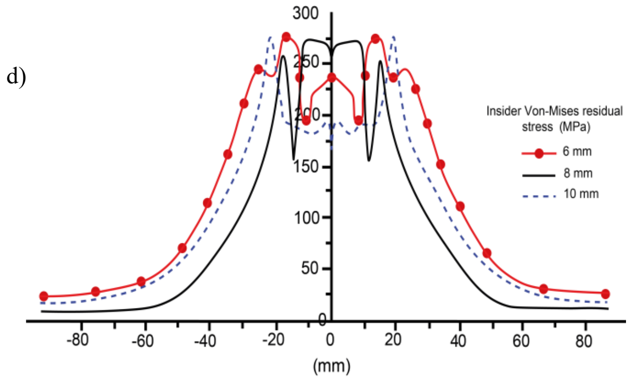

Figure 8. Distribution of residual stresses across pipe thicknesses of 6, 8, and 10 mm for two-pass welding conditions: a) axial stress patterns on outer surface; b) axial stress patterns on inner surface; c) von Mises stress profile on outer surface; and d) von Mises stress profile on inner surface. All measurements are taken at 45° angle from the weld start position.

CONCLUSIONS

In this study, a numerical model is developed using ABAQUS® software to analyse temperature fields and residual stress states in multi-pass TIG welding of AISI 304 stainless steel pipes. Following the validation of the proposed model, the effects of welding speed and pipe thickness on axial stresses for both internal and external surfaces of the AISI 304 pipe are investigated. Key findings include:

- At the weld centre, while the axial stress on the inner surface is tensile, it is compressive on the outer surface. As distance from the weld centre increases, stress values initially decrease, and then the stress type inversely transitions between tensile and compressive.
- Maximum axial stress on the pipe decreases with increasing welding speed. Additionally, the width of the stressed zone narrows at higher welding speeds.
- Heat input has a minimal influence on axial stress, but it significantly impacts stress distribution. For instance, a 40 % increase in heat input results in approximately a 5 % change in peak axial stress, while causing 20 to 40 % variations in overall stress levels, depending on stress type (compression or tension) and position (inside or outside of the pipe).
- Heat input has a minimal influence on axial stress, but it significantly impacts stress distribution. For instance, a 40 % increase in heat input results in approximately a 5 % change in peak axial stress, while causing 20 to 40 % variations in overall stress levels, depending on stress type (compression or tension) and position (inside or outside of the pipe).

These findings provide valuable insights for optimising welding parameters and predicting residual stress distributions in AISI 304 pipe welding applications. The developed model and methodology can be extended to other materials and welding configurations, offering a cost-effective approach for predicting and controlling residual stresses in industrial welding processes. This work contributes to the advancement of welding process optimisation and quality control in critical applications where structural integrity is paramount.

REFERENCES

1. Zala, A.B., Jamnapara, N.I., Badheka, V.J., et al. (2019), *Effect of aluminide coatings on penetration and microstructure of TIG welded 9Cr-1Mo steel for fusion blanket applications*, Fusion Eng. Des. 144: 172-179. doi: 10.1016/j.fusengdes.2019.04.080
2. Naik, A.B., Reddy, A.C. (2018), *Optimization of tensile strength in TIG welding using the Taguchi method and analysis of variance (ANOVA)*, Therm. Sci. Eng. Progress, 8: 327-339. doi: 10.1016/j.tsep.2018.08.005
3. Abbasi, M., Givi, M., Bagheri, B. (2020), *New method to enhance the mechanical characteristics of Al-5052 alloy weldment produced by tungsten inert gas*, Proc. of the Inst. Mech. Eng. Part B: J Eng. Manuf. 239(11): . doi: 10.1177/0954405420929777
4. Đorđević, B., Vučetić, F., Sedmak, A., et al. (2023), *Welding joint made of two different austenitic materials*, Mater. Sci. Forum, 1095: 125-132. doi 10.4028/p-4c1vln
5. Sarmast, A., Serajzadeh, S., Kokabi, A.H. (2014), *A study on thermal responses, microstructural issues, and natural aging in gas tungsten arc welding of AA2024-T4*, Proc. Inst. Mech. Eng. Part B: J Eng. Manuf. 228(3): 413-421. doi: 10.1177/0954405413501669
6. Rasti, A., Sattarifar, I., Salehi, M., Karimnia, V. (2016), *Stress analysis of welded joints in internal stiffener rings in an aluminum cylinder*, Proc. Inst. Mech. Eng. Part L: J Mater.: Des. Appl. 230(1): 121-130. doi: 10.1177/1464420714549064
7. Asadi, P., Alimohammadi, S., Kohantorabi, O., et al. (2020), *Effects of material type, preheating and weld pass number on residual stress of welded steel pipes by multi-pass TIG welding (C-Mn, SUS304, SUS316)*, Therm. Sci. Eng. Prog. 16: 100462. doi: 10.1016/j.tsep.2019.100462
8. Smith, M.C., Bouchard, P.J., Turski, M., et al. (2012), *Accurate prediction of residual stress in stainless steel welds*, Comput. Mater. Sci. 54(1): 312-328. doi: 10.1016/j.commatsci.2011.10.024
9. Xu, S., Wang, W. (2013), *Numerical investigation on weld residual stresses in tube-to-tube sheet joint of a heat exchanger*, Int. J Pres. Ves. Pip. 101: 37-44. doi: 10.1016/j.ijpvp.2012.10.004
10. Deng, D., Murakawa, H. (2006), *Numerical simulation of temperature field and residual stress in multi-pass welds in stainless steel pipe and comparison with experimental measurements*, Comput. Mater. Sci. 37(3): 269-277. doi: 10.1016/j.commatsci.2005.07.007
11. Velaga, S.K., Ravisankar, A. (2017), *Finite element based parametric study on the characterization of weld process moving heat source parameters in austenitic stainless steel*, Int. J Pres. Ves. Pip. 157: 63-73. doi: 10.1016/j.ijpvp.2017.09.001
12. Genchev, G., Doynov, N., Ossenbrink, R., et al. (2017), *Residual stresses formation in multi-pass weldment: A numerical and experimental study*, J Constr. Steel Res. 138: 633-641. doi: 10.1016/j.jcsr.2017.08.017
13. Sedmak, S., Jovičić, R., Sedmak, A., et al. (2017), *Numerical analysis of different weld geometries of lap welded joint in ammonia transport tanks*, Struct. Integr. Life, 17(3): 217-220.
14. Sedmak, S., Jovičić, R., Sedmak, A., et al. (2018), *Influence of multiple defects in welded joints subjected to fatigue loading according to SIST EN ISO 5817:2014*, Struct. Integr. Life, 18 (1): 77-81.
15. Djordjevic, B., Sedmak, S., Tatic, U., et al. (2017), *Measuring of strain and displacements in welded joints subjected to tensile load using stereometric methods*, In: Appl. Mech., Behavior of Mater., and Eng. Systems: Selected contributions to the 5th Algerian Congress of Mechanics, CAM2015, El-Oued, Algeria, Springer Int. Publ. 2017, pp.117-127.
16. Dikić, S., Sedmak, S., Aranđelović, M., et al. (2024), *Numerical and metallographic analysis of a welded joint with microcrack in the root*, In: Proc. of the 12th Annual Conf. of Society for Structural Integrity and Life -DIVK12, Belgrade, 2024, p.147. ISBN 978-86-900686-2-3
17. Petrović, A., Momčilović, N., Đorđević, B., et al. (2025), *Inverse iterative methodology for welded joints characterization in construction designing and comparison to classical approach*, Acta Polytechnica Hungarica, 22(4): 45-63. doi: 10.12700/APH.22.4.2025.4.4
18. Arandjelovic, M., Djordjevic, B., Sedmak, S., et al. (2024), *Failure analysis of welded joint with multiple defects by extended Finite Element Method and Engineering Critical Analysis*, Eng. Fail. Anal. 160: 108176. doi: 10.1016/j.engfailanal.2024.108176
19. Khiari, M.E.A., Mokhtari, M., Telli, F., et al. (2024), *Damage investigation of a pressurized elbow pipe using the XFEM technique under severe cyclic loading*, Mech. Adv. Mater. Struct. 31(26): 7812-7824. doi: 10.1080/15376494.2023.2250535
20. Telli, F., Khiari, M.E.A., Mokhtari, M., et al. (2025), *Damage analysis in welded steel pipe elbow under strong cyclic loading*, Mech. Adv. Mater. Struct. 32(12): 2703-2717. doi: 10.1080/15376494.2024.2383998
21. Obeid, O., Alfano, G., Bahai, H., Jouhara, H. (2017), *A parametric study of thermal and residual stress fields in lined pipe welding*, Therm. Sci. Eng. Prog. 4: 205-218. doi: 10.1016/j.tsep.2017.10.011
22. Asadi, P., Alimohammadi, S., Kohantorabi, O., et al. (2020), *Numerical investigation on the effect of welding speed and heat input on the residual stress of multi-pass TIG welded stainless steel pipe*, Proc. Inst. Mech. Eng., Part B: J Eng. Manuf. 235(6-7): 1007-1021. doi: 10.1177/0954405420981335